



# Design and syntheses of MOF/COF hybrid materials via postsynthetic covalent modification: An efficient strategy to boost the visible-light-driven photocatalytic performance

Fei Li<sup>a</sup>, Dengke Wang<sup>a</sup>, Qiu-Ju Xing<sup>a</sup>, Gang Zhou<sup>a</sup>, Shan-Shan Liu<sup>a</sup>, Yan Li<sup>b</sup>, Ling-Ling Zheng<sup>a</sup>, Peng Ye<sup>a</sup>, Jian-Ping Zou<sup>a,\*</sup>

<sup>a</sup> Key Laboratory of Jiangxi Province for Persistent Pollutants Control and Resources Recycle, Nanchang Hangkong University, Nanchang 330063, P. R. China

<sup>b</sup> School of Chemistry & Molecular Engineering, East China University of Science and Technology, Shanghai 200237, P. R. China



## ARTICLE INFO

### Keywords:

Covalent organic frameworks  
Hydrogen evolution  
Metal-organic frameworks  
MOF/COF hybrid material  
Photocatalysis

## ABSTRACT

The search of novel visible-light-responsive porous materials is important because they hold great promise for applications in various fields. Herein, we report a novel strategy based on postsynthetic covalent modification for fabrication of hierarchical porous metal-organic frameworks/covalent organic frameworks (MOF/COF) hybrid materials. For the first time, benzoic acid-modified covalent triazine-based frameworks (B-CTF-1) are covalently bonded with MOFs ( $\text{NH}_2\text{-MIL-125(Ti)}$  or  $\text{NH}_2\text{-UiO-66(Zr)}$ ) by using this strategy. Photocatalytic results show that the hydrogen production rate over 15 wt%  $\text{NH}_2\text{-MIL-125(Ti)}/\text{B-CTF-1}$  (15TBC) is  $360 \mu\text{mol}\cdot\text{h}^{-1}\cdot\text{g}^{-1}$  under visible light irradiation, which is more than twice as much as that of the B-CTF-1. Meanwhile, the hybrid materials show higher stability as compared to the simple heterostructures of MOFs and COFs connected via Van der Waals force. Photoelectrochemical analyses and controlled experiments indicate that the superior photocatalytic performance of the MOF/COF hybrids can be attributed to the formation of amide bonds between B-CTF-1 and MOFs, which facilitate the charge separation efficiency and improve the stability of the photocatalyst. Finally, a possible mechanism to well explain the improved photocatalytic performance of the photocatalytic system was proposed. The present work provides a new idea to construct highly efficient and stable MOF/COF hybrid systems and broaden the applications of COF-based materials.

## 1. Introduction

Porous organic frameworks (POFs), especially metal-organic frameworks (MOFs) and covalent organic frameworks (COFs), have shown potential applications in catalysis [1–6], gas sorption and separation [7–9] because of their excellent properties, including large surface area, tunable pore architectures and topological structure diversity [10]. In recent years, in order to improve the performance of the single-handed material, MOF-based hybrid materials have been prepared by hybridizing MOFs with other functional materials, such as metal oxides/nanoparticles [11,12], enzymes [13,14], metal porphyrins [15], MOFs [16–22], and COFs [23–25], which could possess the structural traits of individual components and exhibit new properties. For example,  $\text{NH}_2\text{-MIL-68@TPA-COF}$  core-shell hybrid materials have recently been reported and demonstrated to be effective for photocatalytic dyes degradation under visible light [24].

Compared with MOFs, COF-based hybrid materials still remain

largely unexplored. Till now, only three kinds of COF-based hybrid materials have been reported. The first case is the MOF/COF of [COF-300]/[ZIF-8] composite membrane that has good performance of gas separation for  $\text{H}_2/\text{CO}_2$  [26]. The second one is a two-dimensional/three-dimensional triazine porous polymer, which was prepared by a one-pot method for photocatalytic hydrogen production [27]. The third one is  $\text{Fe}_3\text{O}_4@\text{TpBD}$  core-shell hybrid materials that have good photo-thermal conversion capabilities [28]. Although the above COF-based hybrid materials exhibit good performance, the combination modes between COF and the other one among the COF-based hybrid materials are Van der Waals forces or hydrogen bonds, leading to poor stability of the hybrid materials. Therefore, it is urgent to develop a new strategy to obtain novel COF-based hybrid materials with high stability and excellent physicochemical properties.

Herein, we proposed a novel strategy to prepare one new kind of well-defined and hierarchical COF-based hybrid materials by postsynthetic covalent modification method. The COF-based hybrid

\* Corresponding author at: Tel.: +86-791-83953378.

E-mail address: [zjp\\_112@126.com](mailto:zjp_112@126.com) (J.-P. Zou).

materials are consisted of covalent triazine-based frameworks (CTF-1) modified with benzoic acid fragment (B-CTF-1) and NH<sub>2</sub>-MIL-125(Ti) or NH<sub>2</sub>-UiO-66(Zr). Noteworthily, the connections between COFs and MOFs by chemically covalent amide bonds were demonstrated for the first time that such type of connection can not only improve the stability of the catalyst, but it also can enhance the photocatalytic activity by boosting the effective separation of photo-induced charges. The photocatalytic activity of hydrogen evolution was investigated over the resultant hybrids and the mechanism for the hydrogen evolution was also proposed.

## 2. Experimental section

All of the chemicals were commercially available and used without further purification.

### 2.1. Synthesis of CTF-1

Pre-CTF was synthesized by thermal oxidation method according to the previous work [29]. Typically, trifluoromethanesulfonic acid (19.96 g, 133.0 mmol, 4 eq) was added into a pre-dried three-neck round bottom flask containing CHCl<sub>3</sub> (30 mL) under inert gas atmosphere. Then, 1,4-dicyanobenzene (4.26 g, 33.25 mmol) dissolved in CHCl<sub>3</sub> (200 mL) was slowly dropwised into above resulted mixture at 0 °C under stirring. The mixture was stirred for 2 h at 0 °C and then heated to 40 °C for 48 h. A solid precipitate turned from colorless to yellow was formed. After cooled down to room temperature, the solid precipitate was rapidly added to 660 mL of deionized water containing 34 mL of ammonia solution (25%), and then continuously stirred for 2 h. The precipitate was obtained by filtration and washed successively with deionized water, ethanol, acetone and chloroform. The yellow product was dried under vacuum for 12 h at 120 °C. The yellow precipitate regards as Pre-CTF. Pre-CTF (2.100 g, 16.39 mmol, 1 eq) was thoroughly mixed with ZnCl<sub>2</sub> (1.787 g, 13.11 mmol, 0.8 eq) in an inert argon atmosphere. This large batch of starting reaction mixture was evenly separated into 6 parts which were each transferred to a porcelain crucible with lid and stored in a closed storage box to maintain the inert argon atmosphere. After preheating the argon oven for 30 min under a regulated argon flow of 2.5 °C/min to 400 °C, the crucibles were quickly placed into the argon oven and heated at 400 °C for 10 min. The crucibles were immediately removed from the hot oven and allowed to quickly cool down under argon atmosphere. The crude products were grounded and stirred in deionized water (150 mL) for 12 h at 60 °C, filtered and washed thoroughly with water to remove the majority of the salt. The mixtures were further stirred in 0.1 M HCl (150 mL) for 12 h at 60 °C to remove the residual ZnCl<sub>2</sub>, filtered and subsequently washed with water and THF. The product was dried under vacuum for 12 h at 150 °C.

### 2.2. Synthesis of benzoic acid-functionalized CTF-1 nanosheets (B-CTF-1)

Chemical grafting modification method was used to prepare B-CTF-1. Typically, the phenyl carboxylic diazonium salt was pre-fabricated through the following steps: 7 mmol of sodium hydroxide and 960 mg of 4-aminobenzoic acid were added to water and stirred until completely dissolved. Then, 7.6 mmol of sodiumnitrite was slowly added to the above solution under the temperature maintained at 0–5 °C. This solution was rapidly added to 6 M HCl solution with concentration of 20% and stirred for 45 min. The prepared CTF-1 nanosheets (100 mg) was added to the deionized water (200 mL) and ultrasound for 1 h. The as-synthesized diazonium salt was added to the CTF-1 suspension solution, and was stirred for 4 h at 0–5 °C in ice bath. Finally, the solution was filtered and washed several times with distilled water, ethanol, DMF, and acetone, respectively. The final powder was dried at 60 °C for 12 h under vacuum.

### 2.3. Synthesis of NH<sub>2</sub>-MIL-125(Ti)

NH<sub>2</sub>-MIL-125(Ti) was synthesized by a modified method reported in the literature. 2-Aminoterephthalic acid (NH<sub>2</sub>-BDC) (0.5 g, 3 mmol) was added into a dimethylformamide (DMF) (9 mL) and MeOH (1 mL) solution under magnetic stirring. And then tetra-*n*-butyltitantate Ti (OC<sub>4</sub>H<sub>9</sub>)<sub>4</sub> (0.26 mL, 0.75 mmol) was also added into the above mixed solution and stirred at room temperature for 30 min. Then the mixed solution was transferred into a 50 mL Teflon liner and maintained at 150 °C for 72 h. Finally, the purified product was washed several times by DMF and MeOH, and dried overnight at 60 °C vacuum.

### 2.4. Synthesis of the xTBC composites

A certain amount of NH<sub>2</sub>-MIL-125(Ti) and B-CTF-1 powder was placed into 3-neck round bottom flask and 5 mL dry DMF was added, a uniform dispersion of the mixture was obtained by bath sonication under an inert atmosphere. To the above dispersion, N-(3-dimethylaminopropyl)-N'-thylcarbodiimidehydrochloride (EDC.HCl, 20 mg), and 1-hydroxybenzotriazole (HOBt, 20 mg) were added along with N,Ndiisopropylethylamine (DIPEA, 300 µL), ultrasound assisted for one hour stirred at room temperature for 48 h. Finally, the samples were dried at 60 °C under vacuum. Hereafter, the obtained samples of NH<sub>2</sub>-MIL-125(Ti)/B-CTF-1 composed of 10, 15, and 20 wt% NH<sub>2</sub>-MIL-125(Ti) were denoted as 10TBC, 15TBC, and 20TBC, respectively.

### 2.5. Synthesis of simple 15 wt% NH<sub>2</sub>-MIL-125(Ti)/CTF-1 (15T/C) and 15 wt% NH<sub>2</sub>-MIL-125(Ti)/B-CTF-1 (15T/BC) heterostructures

In order to compare the photocatalytic performance of NH<sub>2</sub>-MIL-125(Ti) combined with CTF-1 and B-CTF-1 via covalent bonds and weak interactions, some composite photocatalysts were prepared by the same method in absence of condensation agent. The 15 wt% NH<sub>2</sub>-MIL-125(Ti)/CTF-1 and 15 wt% NH<sub>2</sub>-MIL-125(Ti)/B-CTF-1 represent the composite catalysts, among which NH<sub>2</sub>-MIL-125(Ti) was combined with CTF-1 and B-CTF-1 via weak interactions but not covalent bonds of amide, respectively. The synthetic processes of 15 wt% NH<sub>2</sub>-MIL-125(Ti)/CTF-1 and 15 wt% NH<sub>2</sub>-MIL-125(Ti)/B-CTF-1 are same to that of 15TBC except for the use of condensation agent. The 15 wt% NH<sub>2</sub>-MIL-125(Ti)/CTF-1 and 15 wt% NH<sub>2</sub>-MIL-125(Ti)/B-CTF-1 were denoted as 15T/C and 15T/BC, respectively.

### 2.6. Synthesis of NH<sub>2</sub>-UiO-66(Zr)

NH<sub>2</sub>-UiO-66(Zr) was prepared according to the reported protocol, with slight modifications. NH<sub>2</sub>-BDC (0.19 g, 1.05 mmol) and ZrCl<sub>4</sub> (0.243 g, 1.05 mmol) dissolved in 12 mL of DMF, stirred until completely dissolved, transferred to 25 mL Teflon lining in oven at 120 °C for 24 h. Centrifugation (6000 rpm 15 min) rinses with methanol to remove unreacted H<sub>2</sub>BDC–NH<sub>2</sub> and residual DMF in the wells. The washing step was repeated for 3 days, soaked in methanol daily, and the NH<sub>2</sub>-UiO-66(Zr) powder was vacuum dried at 120 °C for 12 h.

Synthesis of the 15ZBC composites: The synthetic procedures of 15ZBC are similar to that of 15TBC composites except for the use of NH<sub>2</sub>-UiO-66(Zr) instead of NH<sub>2</sub>-MIL-125(Ti).

Synthesis of 15 wt% NH<sub>2</sub>-UiO-66(Zr)/CTF-1 (15Z/C): The synthetic procedures of 15Z/C are similar to that of 15T/C composites except for the use of NH<sub>2</sub>-UiO-66(Zr) instead of NH<sub>2</sub>-MIL-125(Ti).

### 2.7. Characterizations

The crystal phase was determined by X-ray diffraction (Bruker D8CEVANCE) using graphite monochromatized Cu Ka ( $\lambda = 1.5406 \text{ \AA}$ ) radiation. The XRD data for indexing and cell-parameter calculations were collected in a scan mode with a scanning speed of 2°/min in the 2θ range between 5° and 55°. Optical properties were analyzed by using

UV-vis diffuse reflectance spectra (DRS, Varian Cary 300) and photoluminescence spectra (F-7000, Hitachi, Japan) at room temperature. Electrochemical Impedance Spectroscopy (EIS) was carried out in  $\text{Na}_2\text{SO}_4/\text{K}_3(\text{Fe}(\text{CN})_6)/\text{K}_4(\text{Fe}(\text{CN})_6)$  ( $\text{Na}_2\text{SO}_4 = 0.5 \text{ M}$ ,  $\text{K}_3(\text{Fe}(\text{CN})_6) = 0.25 \text{ mM}$  and  $\text{K}_4(\text{Fe}(\text{CN})_6) = 0.25 \text{ mM}$ ) solution over the frequency ranging from 0.01 Hz to 100 kHz at 0.24 V, and the amplitude of the applied sine wave potential in each case was 5 mV. Fourier transformed infrared (FTIR) spectra of the samples were performed by a VERTEX-70 spectrometer, and KBr was used as a blank control. The element composition of catalysts was identified by X ray photoelectron spectroscopy (XPS) (VG 250 Escalabspectrometer and Al-K = 1486.7 eV). Electrochemical measurements were performed on a CHI 660D electrochemical workstation (Shanghai Chenhua, China) using a standard three-electrode cell with a working electrode, a standard calomel electrode as reference electrode, and a graphite electrode as counter electrode. Then the samples were dip-coated onto a 1 cm × 1 cm fluorine-tin oxide (FTO) glass electrode. 0.5 M  $\text{Na}_2\text{SO}_4$  was used as the electrolyte. Inductively Coupled Plasma Optical Emission Spectrometer 720A (ICP-OES 720A). Thermogravimetric analysis (TGA) curves were measured by using a SDT Q600 thermogravimetric analyzer from room temperature to 980 °C with heating rate of 10 °C/min and an air flow rate of 100 mL/min.

### 2.8. Test of photocatalytic activity

All photocatalytic  $\text{H}_2$  evolution experiments were performed via a Pyrex top-irradiation reaction vessel connected to a glass closed gas system (Prefect Light, Beijing, Labsolar-III (AG) in a Pyrex flask) (Fig. S1). A 300 W Xe lamp (Perfect light PLS-SXE300C; Wavelength range:  $420 \text{ nm} \leq \lambda \leq 780 \text{ nm}$ , light intensity:  $160 \text{ mW/cm}^2$ ) was used as the simulated sunlight source. The as-prepared catalyst (20 mg) was uniformly dispersed by using a magnetic stirrer in 80 mL of aqueous solution (containing  $\text{H}_2\text{O}/\text{triethanolamine}$ , v/v = 72:8). Then 3% Pt nanoparticles were deposited as co-catalysts, which were rooted in  $\text{H}_2\text{PtCl}_6$  by a photodeposition method. The system was vacuum-treated several times to remove the dissolved air. The visible-light (> 420 nm) irradiation by a cutoff filter was used to photocatalytic splitting water, and then the amount of produced hydrogen was analyzed by an online gas chromatograph (GC7900). Meanwhile, the cooling water was used to maintain the temperature at 6 °C. In order to ensure the reliability of the experimental results, the experiments of photocatalytic hydrogen evolution were repeated three times and the final values shown in the text are the mean values of triplicate results.

## 3. Results and discussion

CTF-1, a two-dimensional triazine-containing porous organic framework, was chosen in this study as host matrix to immobilize MOF nanoparticles due to its good resistance to water and organic solvents. CTF-1 was prepared from terephthalonitrile via a polymerization method according to previously reported procedures with slight modifications. Among them,  $\text{ZnCl}_2$  salt melt was used as reaction medium in the synthesis of CTF-1, because the pre-CTF-1 can be transformed into an ordered CTF-1 in the salt melt of  $\text{ZnCl}_2$  [29]. The as-synthesized product shows similar XRD patterns and FTIR spectra to those reported previously (Fig. 1), suggesting that CTF-1 with high quality was obtained [29]. The assembly of MOF-modified CTF-1 hybrid materials was prepared via a step-by-step postsynthetic covalent modification method (Scheme 1). The first step of the hybrid preparation involves the modification of CTF-1 with 4-aminobenzoic acid through a diazo-type reaction process, resulting in the formation of CTF-1 composite surface grafting with benzoic acid (B-CTF-1) [30]. The benzoic acid covalently connected to the CTF-1 plays an important role in the preparation of MOF-functionalized COF-based hybrid since it not only tightly adheres the CTF-1 sheet but also provides a functional surface with dense carboxyl group, which can further react with amine groups to produce a

defect-free MOF/COF hybrid materials. The second step refers to the condensation between MOFs and benzoic acid-functionalized CTF-1 to form MOF-modified CTF-1 hybrid materials. In current experiment, amino-functionalized Ti-based  $\text{NH}_2\text{-MIL-125(Ti)}$  was chosen as objective due to its high thermal and chemical stability and its amino functional group for further chemical modifications. In addition,  $\text{NH}_2\text{-MIL-125(Ti)}$  is widely studied and has shown a variety of photocatalytic applications [31–33].  $\text{NH}_2\text{-MIL-125(Ti)}$  was prepared by using 2-aminoterephthalic acid ( $\text{NH}_2\text{-BDC}$ ) as organic linker according to the previously reported method [33], and the XRD pattern and FTIR spectra of the as-synthesized product confirmed that  $\text{NH}_2\text{-MIL-125(Ti)}$  with high quality was obtained (Fig. 1). By blending  $\text{NH}_2\text{-MIL-125(Ti)}$  with benzoic acid-functionalized B-CTF-1 in the presence of N-(3-dimethylaminopropyl)-N'-thylcarbodiimide hydrochloride, 1-hydroxybenzotriazole and N,N-diisopropylethylamine under room temperature, the  $\text{NH}_2\text{-MIL-125(Ti)}/\text{B-CTF-1}$  (TBC) hybrid material was obtained as brown powder.

The crystalline structures of the obtained B-CTF-1 and TBC were analyzed by XRD measurement. As shown in Fig. 1a, the B-CTF-1 shows three broad diffraction peaks similar to those observed over the original CTF-1, indicating that surface modification of CTF-1 with benzoic acid fragments did not influence its structure and morphology. As for the 15TBC, the XRD patterns assigned to B-CTF-1 remained unchanged. However, the existence of new characteristic diffraction peaks corresponding to  $\text{NH}_2\text{-MIL-125(Ti)}$  was observed, suggesting the successful fixation of  $\text{NH}_2\text{-MIL-125(Ti)}$  on B-CTF-1 in the 15TBC. As shown in Fig. 1b, the FTIR spectrum of the resultant B-CTF-1 exhibits three peaks at 1346, 1504, and  $2231 \text{ cm}^{-1}$ , comparable to those observed over the pure CTF-1. However, it is noted that in contrast to that of CTF-1, the FTIR spectrum of the B-CTF-1 shows two new peaks appeared at  $1657 \text{ cm}^{-1}$  and  $1722 \text{ cm}^{-1}$ , assigning to the stretching vibration of  $\text{C=O}$  bonds from amide groups and  $-\text{COOH}$  [34–36]. These observations illuminate the successful graft of benzoic acid fragments in B-CTF-1. When the B-CTF-1 was doped with 15 wt%  $\text{NH}_2\text{-MIL-125(Ti)}$ , a typical peak assigned to amide stretching band at  $1675 \text{ cm}^{-1}$  was observed and the peak's intensity significantly increases, whereas the intensity of peak at  $1722 \text{ cm}^{-1}$  corresponding to the  $\text{C=O}$  from  $-\text{COOH}$  obviously decreases. The results demonstrate that  $-\text{COOH}$  in B-CTF-1 was converted to amide group. In other words, the successful integration of  $\text{NH}_2\text{-MIL-125(Ti)}$  with B-CTF-1 and the formation of TBC were achieved.

XPS analyses were carried out to study the surface chemical composition and electronic state of obtained the B-CTF-1,  $\text{NH}_2\text{-MIL-125(Ti)}$ , and TBC hybrid material. As shown in Fig. 2, the XPS spectrum of the 15TBC in the C 1 s region shows four peaks at 284.7, 285.6, 286.8, and 288.8 eV. The peaks at 284.7, 286.8 and 288.8 eV can be assigned to  $\text{sp}^2$ -hybridized  $\text{C=C}$ ,  $\text{C-C}$  and  $\text{C=O}$  bonds, respectively [33,34]. As compared with the  $\text{NH}_2\text{-MIL-125(Ti)}$  and B-CTF-1, the intensity of the peak ascribed to  $\text{C-N}$  bond (285.6 eV) in 15TBC obviously increased. In addition, a slight negative shift of  $\text{C-N}$  bond in 15TBC was observed in comparison with pure  $\text{NH}_2\text{-MIL-125(Ti)}$ . The peak in the N 1 s region of the 15TBC can be deconvoluted into three peaks at 398.7, 399.4 and 402.6 eV, which belong to  $\text{C=N-C}$ ,  $-\text{NH}_2$ , and  $-\text{N}^+$  groups, respectively [34]. Noteworthily, the intensity of the peak corresponding to  $-\text{NH}_2$  group (399.4 eV) in the 15TBC significantly decreased as compared to that of the  $\text{NH}_2\text{-MIL-125(Ti)}$ . The results elucidate that amine groups in  $\text{NH}_2\text{-MIL-125(Ti)}$  were efficiently converted into amide bonds in the presence of B-CTF-1. No obvious changes in O 1 s and Ti 2p regions have been observed (Fig. 2c and d), indicating that the MOF framework was maintained, in consistence with the XRD results (Fig. 1a).

The morphologies of the as-prepared  $\text{NH}_2\text{-MIL-125(Ti)}$ , B-CTF-1, and BTC were investigated by SEM and TEM. The typical SEM image of the obtained  $\text{NH}_2\text{-MIL-125(Ti)}$  demonstrates a granule-like structure, while the B-CTF-1 shows a two-dimensional layered topology (Fig. 3a and b). When the  $\text{NH}_2\text{-MIL-125(Ti)}$  was combined with the B-CTF-1, a hierarchical structure was observed in the as-formed 15TBC (Fig. 3c).

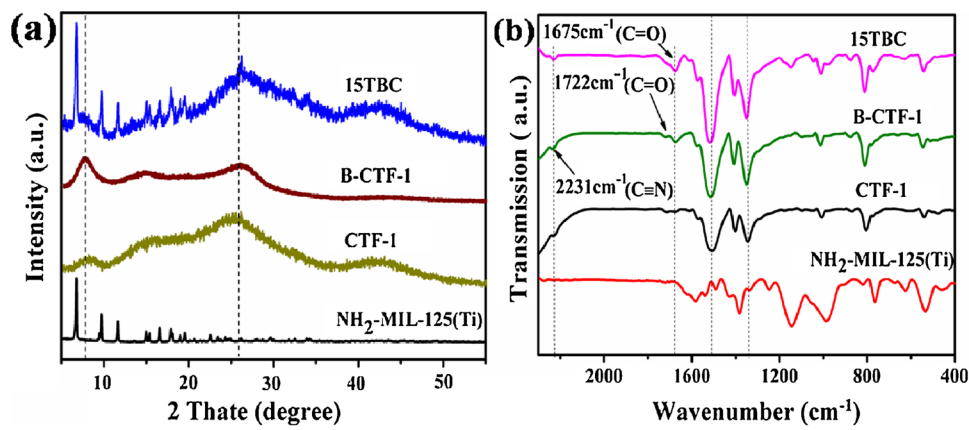


Fig. 1. (a) XRD patterns and (b) FTIR spectra of the as-prepared catalysts.

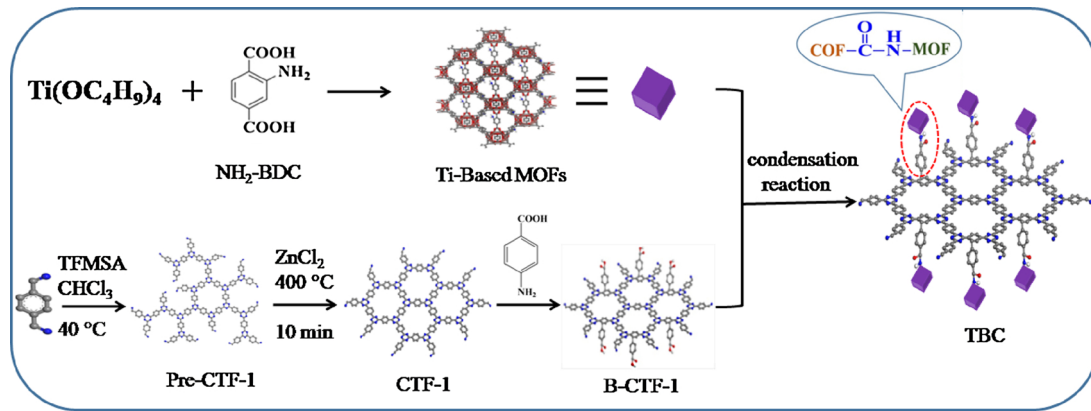
Although the B-CTF-1 sheets in the 15TBC nearly show no differences in comparison to the B-CTF-1, the granular-like morphologies of NH<sub>2</sub>-MIL-125(Ti) have a little change when they combined with the B-CTF-1 sheets, indicating that the NH<sub>2</sub>-MIL-125(Ti) are linked with a certain amount of B-CTF-1 via covalent bonds. The chemically covalent modification of NH<sub>2</sub>-MIL-125(Ti) with B-CTF-1 enables NH<sub>2</sub>-MIL-125(Ti) to highly disperse on the surface of B-CTF-1 sheets. The spatial distribution of different elements in the 15TBC were investigated by elemental mapping analysis (Fig. 4). The N and Ti elements distribution characteristics of 15TBC, which indicated NH<sub>2</sub>-MIL-125(Ti) to highly disperse on the surface of B-CTF-1 sheets. The TEM images of the 15TBC also demonstrate that the NH<sub>2</sub>-MIL-125(Ti) nanoparticles are highly dispersed on the B-CTF-1 sheets, forming hierarchical nanoparticle-on-sheet morphology (Fig. 3d).

Besides the composition and structural characterizations, the optical absorption properties of the prepared samples were studied as shown in Fig. S2. As compared with the NH<sub>2</sub>-MIL-125(Ti) and B-CTF-1, the as-obtained 15TBC shows enhanced light absorption in the 200 nm to 680 nm region, indicating that the chemical conjunction between NH<sub>2</sub>-MIL-125(Ti) and B-CTF-1 in the 15TBC can enhance the visible light absorption.

The flat-band potential of the NH<sub>2</sub>-MIL-125(Ti) determined from Mott-Schottky plots is around  $-1.37$  V vs. SCE, corresponding to  $-1.13$  V vs. the normal hydrogen electrode (NHE), while the flat-band potential of B-CTF-1 is approximately  $-0.84$  V vs. SCE,  $-0.60$  V vs. NHE (Fig. S3b). It is known that the flat-band potential of *n*-type semiconductor equals to the Fermi Level ( $E_F$ ) [37]. Therefore, the  $E_F$  values of NH<sub>2</sub>-MIL-125(Ti) and B-CTF-1 are  $-1.13$  and  $-0.6$  V, respectively. Accordingly, the conduction band (CB) of NH<sub>2</sub>-MIL-125(Ti) and B-CTF-1 can be calculated as  $-1.33$  and  $-0.8$  V, respectively [38]. According to the band gap energy estimated from the DRS spectrum

(Formula in SI), the valence band (VB) potentials of the NH<sub>2</sub>-MIL-125(Ti) and B-CTF-1 are calculated to be  $1.27$  V and  $1.34$  V vs. NHE, respectively (Fig. S3a) [37]. The matched band potentials between B-CTF-1 and NH<sub>2</sub>-MIL-125(Ti) make it theoretically feasible to transfer the photogenerated charges between them, which lead to an effective separation of photogenerated electrons-holes pairs. This is also proved by the results of photocurrent transient response under visible light irradiation. It is obvious that the 15TBC shows the stronger photocurrent intensity than that of the NH<sub>2</sub>-MIL-125(Ti) and B-CTF-1, suggesting the most efficient separation of photoexcited electron-hole pairs owing to the fast charge carriers' transfer between the NH<sub>2</sub>-MIL-125(Ti) and B-CTF-1 (Fig. S4a). In addition, the weakest PL spectra intensity and smallest electrochemical impedance of the 15TBC than that of their neat counterparts indicate the lowest recombination rate of photoexcited charge carriers (Figs. S4b and S4c). These results indicate that the 15TBC hybrid material is expected to be highly efficient in photocatalytic performance.

As a proof-of-concept application, the photocatalytic hydrogen evolution as a model reaction was investigated over the TBC in the presence of triethanolamine as electron donor and Pt as cocatalyst under visible light irradiations ( $\lambda \geq 420$  nm). Fig. 5a shows the photocatalytic hydrogen evolution rate for the TBC as compared to those of the NH<sub>2</sub>-MIL-125(Ti), CTF-1 and B-CTF-1. Only negligible hydrogen was obtained when the NH<sub>2</sub>-MIL-125(Ti) was used as photocatalyst alone, meanwhile a relative low hydrogen evolution rate of  $168$  and  $179 \mu\text{mol h}^{-1}\text{g}^{-1}$  was achieved over the CTF-1 and B-CTF-1, respectively. However, in the presence of the TBC, the hydrogen evolution reaction proceeded smoothly and the loading amount of NH<sub>2</sub>-MIL-125(Ti) in TBC played an important role in this reaction. Among all the TBC hybrids, 15TBC gave the best performance by showing the highest hydrogen evolution activity of  $360 \mu\text{mol h}^{-1}\text{g}^{-1}$ , with apparent



Scheme 1. Schematic illustration of the formation of TBC hybrid material.

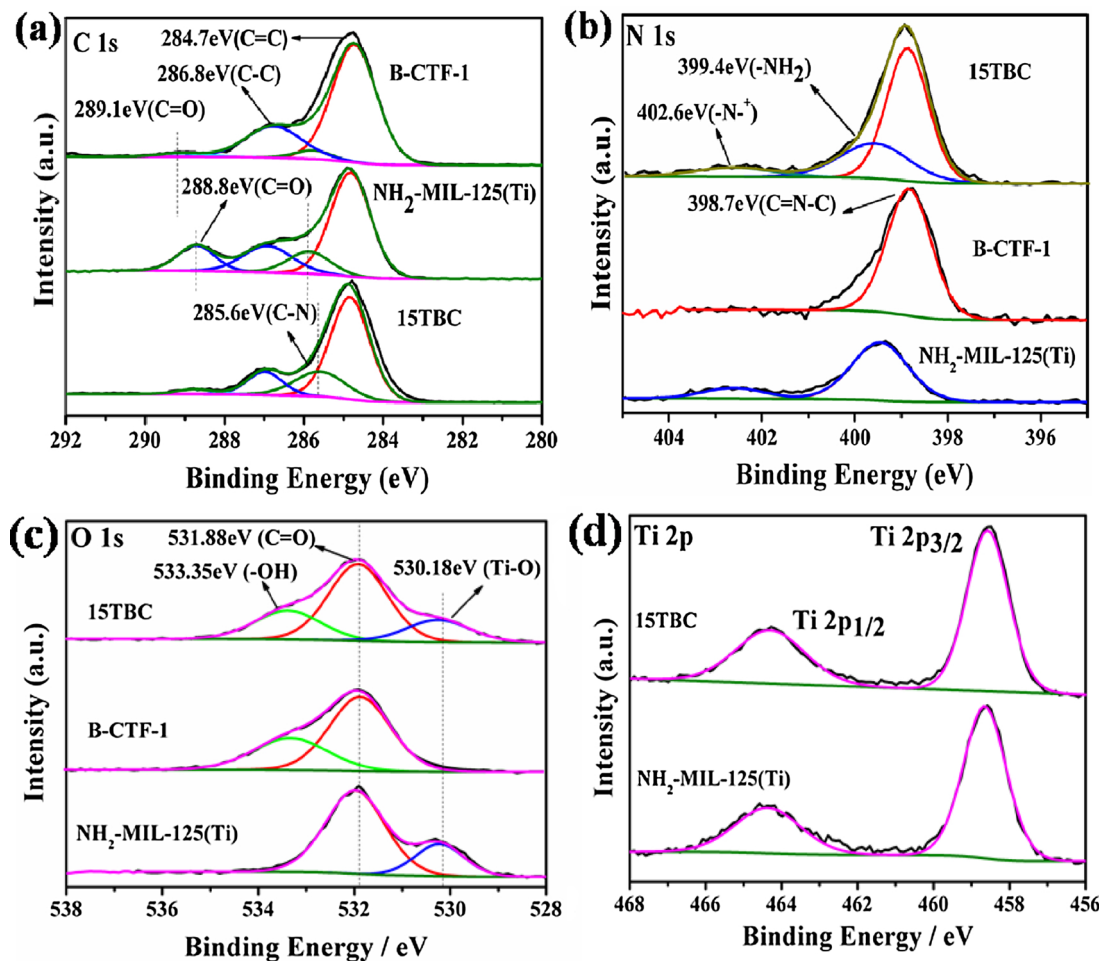


Fig. 2. XPS spectra in (a) C 1s, (b) N 1s, (c) O 1s and (d) Ti 2p for NH<sub>2</sub>-MIL-125(Ti), B-CTF-1, CTF-1 and 15TBC.

quantum efficiency of 0.87% at 420 nm. This hydrogen evolution rate ( $360 \mu\text{mol}\cdot\text{h}^{-1}\cdot\text{g}^{-1}$ ) over the 15TBC is 2.2 and 2.1 times of that over the CTF-1 and the B-CTF-1, respectively, under the same reaction conditions. The superior photocatalytic activity over the hybrid material of the 15TBC indicates that postsynthetic covalent modification of B-CTF-1 with MOF materials is an efficient strategy to improve its photocatalytic activity. Controlled experiments did not give any detectable products in the absence of photocatalysts or light irradiation, indicating that hydrogen evolution is truly induced by the 15TBC under irradiation of visible light.

It is worth noting that the chemical covalent connection between the B-CTF-1 and NH<sub>2</sub>-MIL-125(Ti) via amide bonds is significant for enhancing the photocatalytic activity in the current catalytic system. In order to gain insight into this opinion, the 15 wt% NH<sub>2</sub>-MIL-125(Ti)/CTF-1 (15T/C) and 15 wt% NH<sub>2</sub>-MIL-125(Ti)/B-CTF-1 (15T/BC) were constructed through weak Van der Waals force or hydrogen bonds, and their applications for photocatalytic hydrogen evolution were investigated. It was found that both the 15T/C and 15T/BC exhibited inferior catalytic activities for hydrogen production to the 15TBC under the same reaction conditions. The rates of hydrogen evolution over the 15T/C and 15T/BC were only 132 and 145  $\mu\text{mol}\cdot\text{h}^{-1}\cdot\text{g}^{-1}$ , respectively (Fig. 5b). The superior performance observed over the 15TBC should be ascribed to the as-formed amide bonds that serve as charge mediate and facilitate the separation efficiency of the photogenerated electron-hole pairs at the interface of MOF/COF hybrid.

The 15TBC shows high stability for photocatalytic hydrogen evolution reaction. In contrast to that of the 15T/C and 15T/BC, no obvious loss of the photocatalytic activity was observed over the 15TBC after

four recycling tests (Fig. 5b). The 15TBC after four runs showed unchanged XRD patterns and its FTIR spectra were similar to that of the fresh one (Fig. S5a and S5b). In addition, the TEM image of the used catalyst shows that the NH<sub>2</sub>-MIL-125(Ti) with almost similar distribution were maintained and incorporated with CTF-1 sheets (Fig. S5c). The ICP data of Pt was measured and Pt content is 1.03%. The results suggest that the 15TBC shows high stability during the photocatalytic reaction.

On the basis of the observations described above, the mechanism for photocatalytic hydrogen production over the TBC was proposed (Scheme 2). Upon visible light irradiation, both the NH<sub>2</sub>-MIL-125(Ti) and B-CTF-1 can be excited to generate electrons and holes. According to the results of Mott-Schottky measurements, the matched band potentials between the B-CTF-1 and NH<sub>2</sub>-MIL-125(Ti) is favor for the photogenerated electrons transfer from the CB of the NH<sub>2</sub>-MIL-125(Ti) to the CB of the B-CTF-1 through the amide bridge bonds. Then, the electrons can be further trapped by Pt nanoparticles deposited on the surface of photocatalyst and react with water to produce hydrogen. In this case, holes in the VB of B-CTF-1 migrated to the VB of NH<sub>2</sub>-MIL-125(Ti) and are scavenged by sacrificial agent of triethanolamine to fulfill the photocatalytic cycle.

In our studies, we have noticed that the highly stable aforementioned hybrid material cannot be directly synthesized using the original CTF-1 as the seed, indicating that the surface modification of benzoic acid is a prerequisite for the formation of MOF/COF hybrid materials. Moreover, the efficient postsynthetic covalent modification method in the formation of TBC can also be applied to the preparation of CTF-1 connected by different MOF nanoparticles. For example, when the

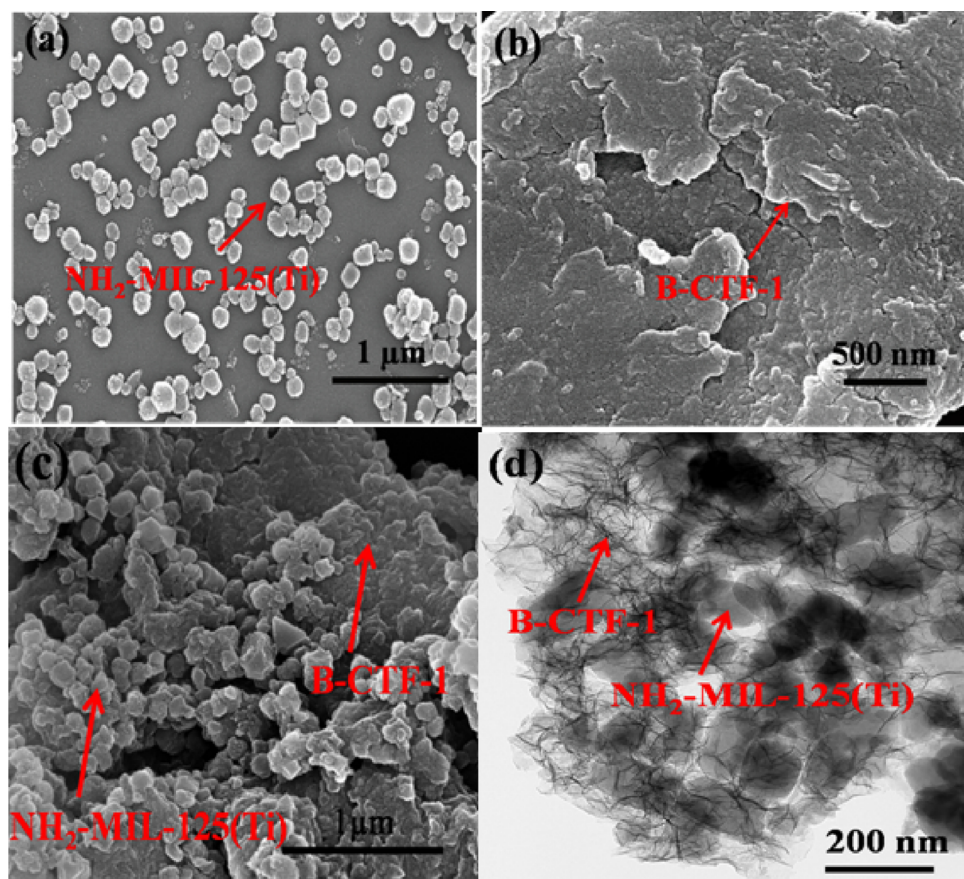


**Fig. 3.** (a-c) SEM images of the  $\text{NH}_2\text{-MIL-125}(\text{Ti})$ , B-CTF-1, and 15TBC, respectively; (d) TEM image of the 15TBC.

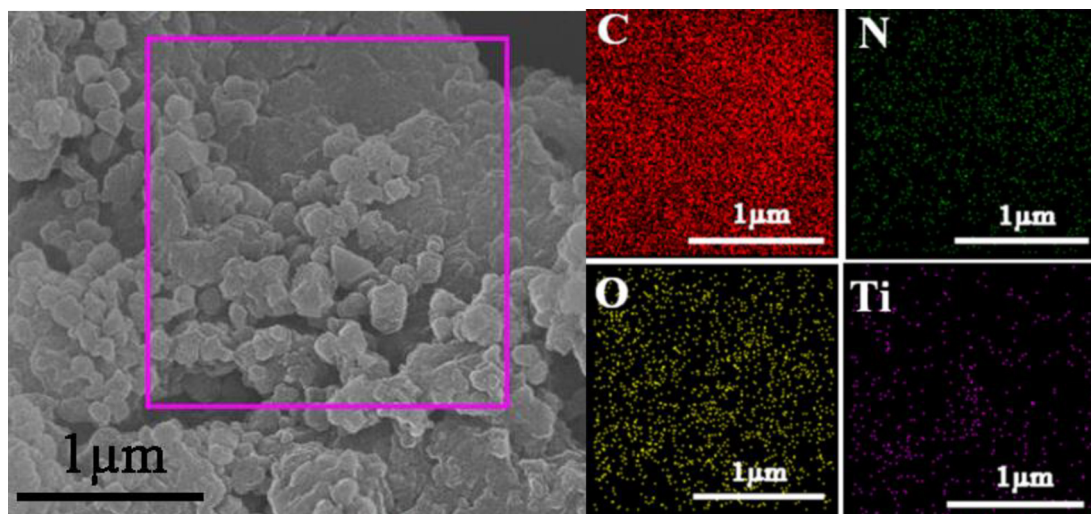


**Fig. 4.** SEM image of the 15TBC and elemental mapping images of C, N, O and Ti.

amine-functionalized  $\text{NH}_2\text{-UiO-66}(\text{Zr})$ , synthesized from  $\text{ZrCl}_4$  and  $\text{NH}_2\text{-BDC}$  as organic ligand, was used as MOF target, the well-defined hierarchical  $\text{NH}_2\text{-UiO-66}(\text{Zr})/\text{B-CTF-1}$  (ZBC) hybrid material was also successfully obtained via a similar postsynthetic covalent modification processes (see the experimental section in the supporting information). The as-obtained ZBC hybrid was characterized by XRD, FTIR and TEM as described in Fig. S6 and S7. Similar to the TBC, the 15ZBC also showed superior photocatalytic activity of hydrogen evolution over their counterparts and higher stability as compared to the 15Z/C, among which  $\text{NH}_2\text{-UiO-66}(\text{Zr})$  was simply connected to CTF-1 through

Van der Waals force (Figs. 5a and S8). In addition, in order to compare the difference between 15TBC and 15ZBC photocatalytic hydrogen production, we conducted a series of photoelectric tests (such as photoluminescence, impedance arc radius, and transient photocurrent responses), which show the 15ZBC has better photocatalytic performance than the 15TBC (Fig. S9). The thermal stability of the as-prepared catalysis was provided in Fig. S10. Compared with  $\text{NH}_2\text{-MIL-125}(\text{Ti})$ ,  $\text{NH}_2\text{-UiO-66}(\text{Zr})$ , and B-CTF-1, 15TBC and 15ZBC have better thermal stability, which could be due to the formation of polar amide covalent bonds between MOFs and CTF-1.

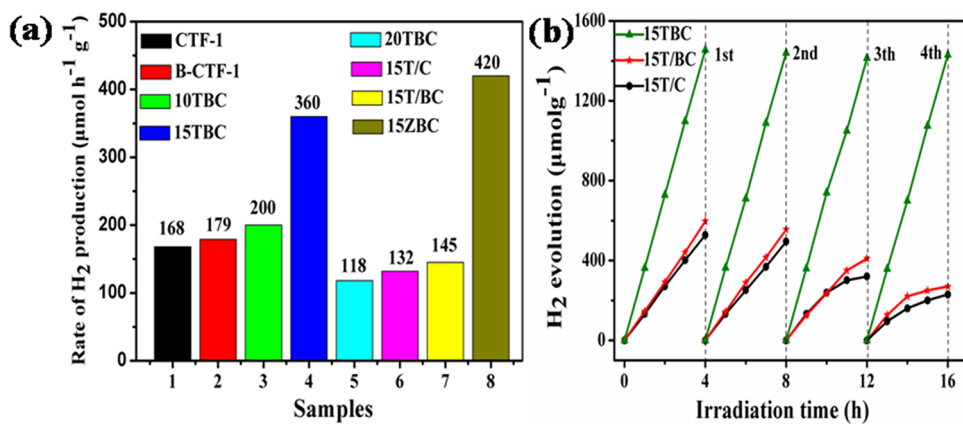
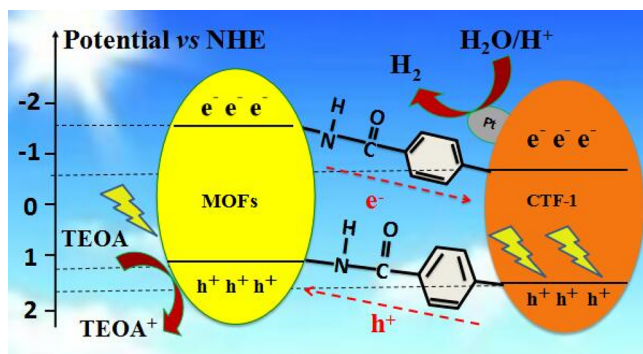


**Fig. 5.** (a) Rate of hydrogen evolution over the different samples under visible light irradiation; (b) Cycling runs of the as-prepared catalysts under visible light irradiation.



**Scheme 2.** Photocatalytic mechanism of the charge transfer for hydrogen evolution over the 15TBC under visible light irradiation.

#### 4. Conclusions

In summary, a facile and effective postsynthetic covalent modification strategy was developed to fabricate hierarchical MOF/COF hybrid material with highly dispersed MOF nanoparticles (for example  $\text{NH}_2\text{-MIL-125(Ti)}$  and  $\text{NH}_2\text{-UiO-66(Zr)}$ ) on COFs (such as benzoic acid modified CTF-1 sheets). The preparation and physicochemical properties of the MOF/COF materials have been systematically studied. Photoelectrochemical analyses indicate that the formation of amide bonds between COFs and MOFs can serve as charge transfer mediator that significantly promote the separation efficiency of electron-hole pairs. As a proof-of-concept, the resultant MOF/COF hybrid can be used as superior and stable photocatalytic system for hydrogen evolution under visible light irradiation. To the best of our knowledge, this is for the first time reported the synthesis of MOF-modified CTF-1 hybrid materials for efficient photocatalytic hydrogen generation. The present work provides a new idea to construct highly efficient and stable MOF/COF hybrid systems, and highlights the great potential of using MOF/COF hybrid materials as catalysts for solar energy conversion.

#### Acknowledgements

We gratefully acknowledge the financial support of the NSF of China (51622806, 51878325, 51868050, 51378246 and 51720105001), the NSF of Jiangxi Province (20162BCB22017, 20165BCB18008, 20171ACB20017, and 20171BAB206049) and the graduate student innovation fund of Jiangxi province (YC2017012).

#### Appendix A. Supplementary data

Supplementary data associated with this article can be found, in the

online version, at <https://doi.org/10.1016/j.apcatb.2018.10.043>.

#### References

- X. Lian, Y. Fang, E. Joseph, Q. Wang, J. Li, S. Banerjee, C. Lollar, X. Wang, H.C. Zhou, Chem. Soc. Rev. 46 (2017) 3386.
- Q. Yang, Q. Xu, H.L. Jiang, Chem. Soc. Rev. 46 (2017) 4774.
- S.M.J. Rogge, A. Bavykina, J. Hajek, H. Garcia, A.I. Olivos-Suarez, A. Sepúlveda-Escribano, A. Vimont, G. Clet, P. Bazin, F. Kapteijn, M. Daturi, E.V. Ramos-Fernandez, F.X. Llabre i Xamena, V. Van Speybroeck, J. Gascon, Chem. Soc. Rev. 46 (2017) 3134.
- A. Dhakshinamoorthy, A.M. Asiri, H. García, Angew. Chem. Int. Ed. 55 (2016) 5414.
- M. Wen, K. Mori, Y. Kuwahara, T. An, H. Yamashita, Appl. Catal. B 218 (2017) 555.
- M. Wen, K. Mori, Y. Kuwahara, Y. Kuwahara, T. An, H. Yamashita, Chem. Asian J. 13 (2018) 1767.
- W.Y. Gao, M. Chrzanowski, S. Ma, Chem. Soc. Rev. 43 (2014) 5841.
- U. Diaz, A. Corma, Coord. Chem. Rev. 311 (2016) 85.
- X. Feng, X.S. Ding, D.L. Jiang, Chem. Soc. Rev. 41 (2012) 6010.
- Z.F. He, W. Jiang, C.A. Schalley, Chem. Soc. Rev. 44 (2015) 779.
- D.K. Wang, Y.T. Pan, L.Z. Xu, Z.H. Li, J. Catal. 361 (2018) 248.
- Y. Huang, M. Zhao, S. Han, Z. Lai, J. Yang, C. Tan, Q. Ma, Q. Lu, J.Z. Chen, X. Zhang, Z. Zhang, B. Li, B. Chen, Y. Zong, H. Zhang, Adv. Mater. 29 (2017) 1700102.
- F.K. Shieh, S.C. Wang, C.I. Yen, C.C. Wu, S. Dutta, L.Y. Chou, J.V. Morabito, P. Hu, M.H. Hsu, K.C.W. Wu, C.K. Tsung, J. Am. Chem. Soc. 137 (2015) 4276.
- D.W. Feng, T.F. Liu, J. Su, M. Bosch, Z.W. Wei, W. Wan, D.Q. Yuan, Y.P. Chen, X. Wang, K.C. Wang, X.Z. Lian, Z.Y. Gu, J. Park, X.D. Zou, H.C. Zhou, Nat. Commun. 6 (2015) 5979.
- C. Wang, D. Liu, W. Lin, J. Am. Chem. Soc. 135 (2013) 13222.
- K. Hirai, S. Furukawa, M. Kondo, H. Uehara, O. Sakata, S. Kitagawa, Angew. Chem. Int. Ed. 50 (2011) 8057.
- T. Li, J.E. Sullivan, N.L. Rosi, J. Am. Chem. Soc. 135 (2013) 9984.
- X. Song, T.K. Kim, H. Kim, D. Kim, S. Jeong, H.R. Moon, M.S. Lah, Chem. Mater. 24 (2012) 3065.
- B. Liu, M. Tu, D. Zacher, R.A. Fischer, Adv. Funct. Mater. 23 (2013) 3790.
- F. Yang, G. Xu, Y. Dou, B. Wang, H. Zhang, H. Wu, W. Zhou, J.R. Li, B.L. Chen, Nat. Energy 2 (2017) 877.
- Z.G. Gu, D.J. Li, C. Zheng, Y. Kang, C. Wçll, J. Zhang, Angew. Chem. Int. Ed. 129 (2017) 6957.
- T. Fukushima, S. Horike, H. Kobayashi, M. Tsujimoto, S. Isoda, M.L. Foo, Y. Kubota, M. Takata, S. Kitagawa, J. Am. Chem. Soc. 134 (2012) 13341.
- D.R. Sun, S.W. Jang, S.J. Yim, L. Ye, D.P. Kim, Adv. Funct. Mater. 28 (2018) 1707110.
- Y.W. Peng, M.T. Zhao, B. Chen, Z.C. Zhang, Y. Huang, F.N. Dai, Z.C. Lai, X.Y. Cui, C.L. Tan, H. Zhang, Adv. Mater. 30 (2018) 1705454.
- Y.H.L. Nguyen, F. Gándara, H. Furukawa, T.L.H. Doan, K.E. Cordova, O.M. Yaghi, J. Am. Chem. Soc. 138 (2016) 4330.
- J.R. Fu, S. Das, G.L. Xing, T. Ben, V. Valtchev, S.L. Qiu, J. Am. Chem. Soc. 138 (2016) 7673.
- D. Schwarz, Y. Noda, J. Klouda, S.P. Karolina, J.J. Tarábek, Rybáček, J. Janouek, F. Simon, M.V. Opanasenko, J. Čejka, A. Acharjya, J. Schmidt, S. Selve, R.S. Valentin, N. Severin, J.P. Rabe, P. Ecorchard, J.J. He, M. Polozij, P. Nachtigall, M.J. Bojdys, Adv. Mater. 29 (2017) 1703399.
- J. Tan, S. Namuangruk, W.F. Kong, K. Nawee, J. Guo, C.C. Wang, Angew. Chem. Int. Ed. 55 (2016) 13979.
- S. Kuecken, A. Acharjya, L. Zhi, M. Schwarze, R. Schomäcker, A. Thomas, Chem. Commun. 53 (2017) 584.
- M. Jahan, Q.L. Bao, J.X. Yang, Kian P. Loh, J. Am. Chem. Soc. 132 (2010) 14487.
- M.B. Chambers, X. Wang, L. Ellezam, O. Ersen, M. Fontecave, C. Sanchez, L. Rozes,

- M.D. Caroline, J. Am. Chem. Soc. 139 (2017) 8222.
- [32] M.A. Nasalevich, C.H. Hendon, J.G. Santaclarra, K. Svane, B.V. Linden, S.L. Veber, M.V. Fedin, A.J. Houtepen, M.A. Veen, F. Kapteijn, A. Walsh, J. Gascon, Sci. Rep. 6 (2016) 23676.
- [33] G. Zhou, M.F. Wu, Q.J. Xing, F. Li, H. Liu, X.B. Luo, J.P. Zou, J.M. Luo, A.Q. Zhang, Appl. Catal. B 220 (2018) 607.
- [34] J. Ma, X.Y. Guo, Y.P. Ying, D.H. Liu, C.L. Zhong, Chem. Eur. J 313 (2017) 890.
- [35] C. Yang, X. You, J.H. Cheng, H.D. Zheng, Y.C. Chen, Appl. Catal. B 200 (2017) 673.
- [36] M.H. Cao, P.F. Wang, Y.H. Ao, C. Wang, J. Hou, J. Qian, Chem. Eur. J 264 (2015) 113.
- [37] X.H. Jiang, Q.J. Xing, X.B. Luo, F. Li, J.P. Zou, S.S. Liu, X. Li, X.K. Wang, Appl. Catal. B 228 (2018) 29.
- [38] J.P. Zou, L.C. Wang, J. Luo, Y.C. Nie, Q.J. Xing, X.B. Luo, H.M. Du, S.L. Luo, S.L. Suib, Appl. Catal. B 193 (2016) 103.